3D modelling of the interaction between bending and corrosion-induced cracks in reinforced concrete beams

Construction and Building Materials 411 (2024) 134272

Contents lists available at ScienceDirect

Construction and Building Materials

journal homepage: www.elsevier.com/locate/conbuildmat

3D modelling of the interaction between bending and corrosion-induced cracks in reinforced concrete beams

Lang-Zi Chang *, Jonathan Thorsson, Karin Lundgren

Department of Architecture and Civil Engineering, Chalmers University of Technology, SE 412 96 Gothenburg, Sweden

ARTICLE INFO

Keywords:
Reinforced concrete
Bending crack
Corrosion-induced crack
3D modelling
Crack pattern
Crack width

ABSTRACT

Bending and corrosion-induced cracks interact and impact the durability of Reinforced Concrete (RC) beams in a complex manner. Still, research on the mechanisms behind this interaction is limited. In this study, a 3D nonlinear finite element modelling method of RC beams was developed to explore this interactive mechanism. The models were assessed against experimental benchmarks, showing good agreement in terms of crack pattern and growth. Moreover, the modelling method offered the advantage of visualising the internal condition of beams, including the propagation of internal cracks and the expansion of corrosion products represented by interface elements. A parametric study was conducted to examine the influence of three crucial factors: the transport of the corrosion products, the distance between bending cracks, and bending crack width. The modelling results revealed that the transport of corrosion products appeared to play a decisive role in the location of initiation and evolution of corrosion-induced cracks. Additionally, as the distance between the bending cracks decreased, the onset of corrosion-induced cracks transitioned from the midpoint between the bending cracks to the vicinity of them. Furthermore, an increase in bending crack width had no impact on the initiation and evolution of corrosion-induced cracks, while their widths, and variation of width along the bar, decreased.

1. Introduction

Given the extensive use of Reinforced Concrete (RC) in global construction, its durability has become increasingly vital in the endeavour to build a sustainable society [1]. Among the various mechanisms that significantly deteriorate the durability of RC structures, corrosion of the reinforcement is a prevalent concern [2–5]. From the perspective of structural engineering, the corrosion of steel reinforcement has two major adverse effects on RC structures: the reduction in the cross-sectional area of steel bars, thereby weakening the overall load-bearing capacity against tensile stresses, and the expansion of corrosion products, which induces splitting stresses in the concrete. The latter effect can lead to the formation of cracks and spalling in the concrete cover, in turn exacerbating the corrosion process, and severely compromising the bond between the steel reinforcement and concrete [6–11]. These effects can reduce the load-carrying capacity of structural components, potentially resulting in structural collapse.

In practice, the corrosion process of RC beams is affected by bending cracks. When subjected to bending actions, the steel reinforcement sections exposed to the external environment at the location of bending cracks tend to corrode first and cause pitting corrosion, which is followed by uniform corrosion along the bars and leads to the formation of corrosion-induced cracks [12,13]. With a demand to enable non-destructive assessment through visual detection, researchers have attempted to establish correlations between the corrosion level of the steel reinforcement and the width of corrosion-induced cracks [14–17]. However, the greatest width of corrosion-induced cracks does not necessarily indicate the most severely corroded sections of the steel bars. In an extensive experiment on corrosion distribution in RC beams under sustained bending loads, Yu et al. [18] found that predicting highly corroded areas based only on crack width is unfeasible. Yet, they also concluded that a strong correlation exists between the maximum width of corrosion-induced cracks and the average cross-sectional loss of the steel reinforcement. Berrocal et al. [12] confirmed experimentally that there was no single unique correlation between corrosion level (usually defined as the loss of cross-sectional area relative to the initial cross-sectional area of rebars) and corrosion-induced crack width. They further observed that the corrosion-induced cracks predominantly originated and exhibited the greatest width in the middle area between bending cracks. Although the testing methods used in these

* Corresponding author.
E-mail address: Langzi.Chang@chalmers.se (L.-Z. Chang).

https://doi.org/10.1016/j.conbuildmat.2023.134272
Received 25 August 2023; Received in revised form 22 October 2023; Accepted 19 November 2023
Available online 25 November 2023

experimental studies do not fully unveil the mechanisms underlying the interaction between bending and corrosion-induced cracks, they underscore the significance of further investigation. Exploring this interaction is essential to gain a profound understanding of the relationship between the corrosion process and crack propagation in RC beams.

Finite element (FE) modelling offers a cost-effective alternative to physical experiments and holds significant potential for studying the intersection between bending and corrosion-induced cracks in RC beams. Initially, FE models primarily simulated rebar corrosion and concrete cracking in 2D space. These models usually represent cross-sections of RC components to depict crack propagation towards the concrete cover [19–21]. However, such 2D models are inadequate for capturing various mechanical behaviours, including corrosion product expansion along rebars, crack propagation in any direction within the concrete, and the combined impact of bending and corrosion product expansion. Fulfilling these objectives necessitates the adoption of 3D models. In recent years, considerable efforts have been dedicated to developing effective 3D models that can accurately capture the corrosion behaviour of RC beams. For instance, Lundgren [22] proposed a constitutive model that considers both the bonding connection between concrete and steel reinforcement and the volume expansion of corrosion products within a single layer of the interface element. The model employed solid elements to represent the steel rebars and concrete. Furthermore, the model was successfully applied to simulate pull-out tests consisting of corroded rebars. In another study, Zandi Hanjari et al. [10] developed the constitutive model so that it incorporates the flow of corrosion products within cracks, pores in concrete, and pits on rebars subjected to high corrosion attacks. This model was utilised to investigate the anchorage of steel reinforcement after corrosion, aligning with experiments conducted on RC beam-ends. Wang et al. [23] proposed an approach to accurately capture the non-uniform distribution of corrosion and the arrangement of stirrups while simulating a concrete cross-section with corroded rebars. Koteš et al. [24] established 3D models to study the influence of stirrups on the RC beams with reinforcements corroded. Other studies with similar objectives can be found in references [25–31]. These studies collectively enable observation and control of corrosion product expansion over time and facilitate monitoring of crack propagation on both external surfaces and within the concrete.

However, based on the authors' knowledge, certain aspects are currently absent or lacking in the state-of-the-art regarding the modelling of corrosion-induced cracks. These include the absence of models accounting for combined bending and corrosion-induced cracks, the lack of a connection between bending cracks and pitting corrosion, and the absence of an investigation into the effect of pitting and uniform corrosion. Moreover, the existing models mainly focus on partial representations of the cross sections of beams, rather than treating beams as whole structural components.

To address the aforementioned gaps and investigate the interaction between bending and corrosion-induced cracks in reinforced concrete (RC) beams, this study establishes a 3D finite element modelling method. The modelling method and assumptions are initially presented, followed by their assessment against experimental campaigns on RC beams with slightly and severely corroded rebars conducted by Berrocal et al. [12] and Yang et al. [13], respectively. A comprehensive comparison is made regarding the crack pattern, its evolution, as well as the time history and width of the cracks. Subsequently, the modelling method is employed to examine three significant factors influencing the interactive behaviour: the transport of corrosion products, the distance between bending cracks, and bending crack width.

2. Establishment of the 3D modelling method

The 3D modelling method in this study encompasses several notable features: it effectively considers the bending action accompanied by expansion of corrosion products; it establishes a connection between bending cracks and pitting corrosion; and it enables the investigation of the relationship between the expansion rates of pitting and uniform corrosion.

Fig. 1 shows an overview of a model representing an ordinary RC beam. The beam was simply supported and subjected to 4-point bending (Fig. 1a). Concrete and bottom rebars were modelled with solid elements, while stirrups and top rebars were simplified as one-dimensional reinforcement elements. The bond mechanism and the expanding behaviour of the rust between the concrete and bottom rebars were modelled with interface elements. Weaker concrete elements with reduced tensile strength were placed along the bottom of the beam to induce bending cracks at the same locations recorded in the experimental results. Pitting and uniform corrosion were distinguished by assigning different corrosion rates to different interface elements. The locations of pitting corrosion were assumed to be the same as the bending cracks, namely those of the weaker concrete (Fig. 1b). This follows the experimental observations that the positions of corrosion pits were in close agreement with the positions of the bending cracks [12, 13]. The pit length in the experiments was defined as the distance where the local corrosion level exceeded the average corrosion level calculated over the mean crack spacing [12]. In the numerical model, the pit length was taken as 20 mm, which equals the average of all individual pit lengths identified in the experiments. To improve computing efficiency, the circular section of the bottom rebars is simplified as an octagon (Fig. 1c). Furthermore, symmetry was utilised, thus only the front half of the beam was modelled with a central symmetric surface supported in the out-of-plane direction. Note that bending cracks were present in all scenarios studied. For scenarios without bending cracks, it would be reasonable to assume pitting corrosion to be randomly distributed along the rebars.

Regarding the material models, Von Mises plasticity with strain hardening was applied to the steel. The total strain crack model was applied to the concrete with exponential softening for tensile behaviour and Thorenfeldt curve for compressive behaviour [32]. The bond-corrosion model applied to the interface elements was proposed by Lundgren [22,33]. With this model, the bond mechanism and expansion of corrosion products between concrete and steel are coupled and assigned to one layer of interface elements (Fig. 2a). The bond part of the model is equivalent to the Coulomb friction with yield functions describing the upper limit. In Fig. 2b, symbols c, μ, σ_n and σ_t are stress in the inclined compressive struts, coefficient of friction, normal splitting stress, and bond stress, respectively. For plastic loading along the yield function describing the upper limit, F_2, an associated flow rule is assumed. For the yield function describing the friction, F_1, a non-associated flow rule is assumed. Details regarding the bond model are referred to [33]. The volume expansion of the corrosion products compared with the uncorroded steel was modelled as an increasing relative normal displacement in the interface elements (Fig. 2a and c). Based on experimental observations, the rust is assumed to behave like a granular material, namely, its stiffness increases with higher stress levels, as shown in Fig. 2d [34]. The constitutive relation between the corrosion penetration x and the normal stress t_n is expressed in Eqs. (1–3), where r is the initial radius of the rebar, x is the corrosion penetration, a is the free increase of the radius, u_{ncor} is the real increase of the radius, ν is the ratio of the rust volume and steel volume, K_{cor} and p are parameters describing the mechanical behaviour of the rust, ε_{cor} and t_n are strain and stress caused by the corrosive products, respectively. More details about the corrosion model are referred to [22].

$$a = -r + \sqrt{r^2 + (\nu - 1) \bullet (2rx - x^2)} \tag{1}$$

$$\varepsilon_{cor} = \frac{u_{ncor} - a}{x + a} \tag{2}$$

$$t_n = K_{cor} \bullet {\varepsilon_{cor}}^p \tag{3}$$

In this study, the geometry was meshed into quadratic 20-node cubic

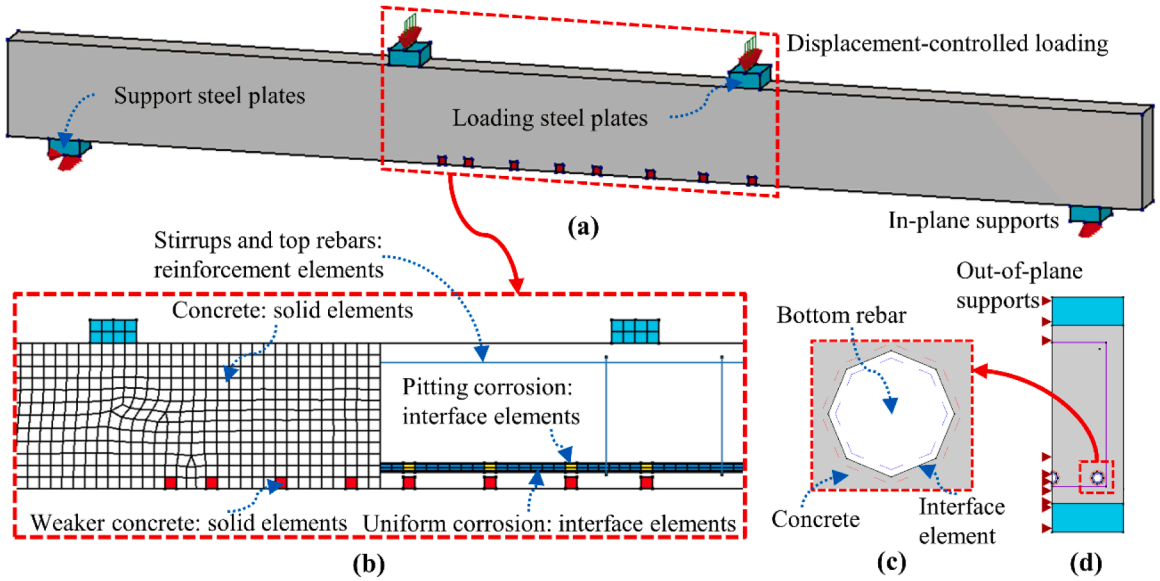

Fig. 1. Overview of a model: (a) geometry, boundary conditions and loading of the 3D representation of the model; (b) elements representing the concrete, interface between concrete and rebars; (c) rebar approximated as octagon; (d) Left elevation of the symmetric model.

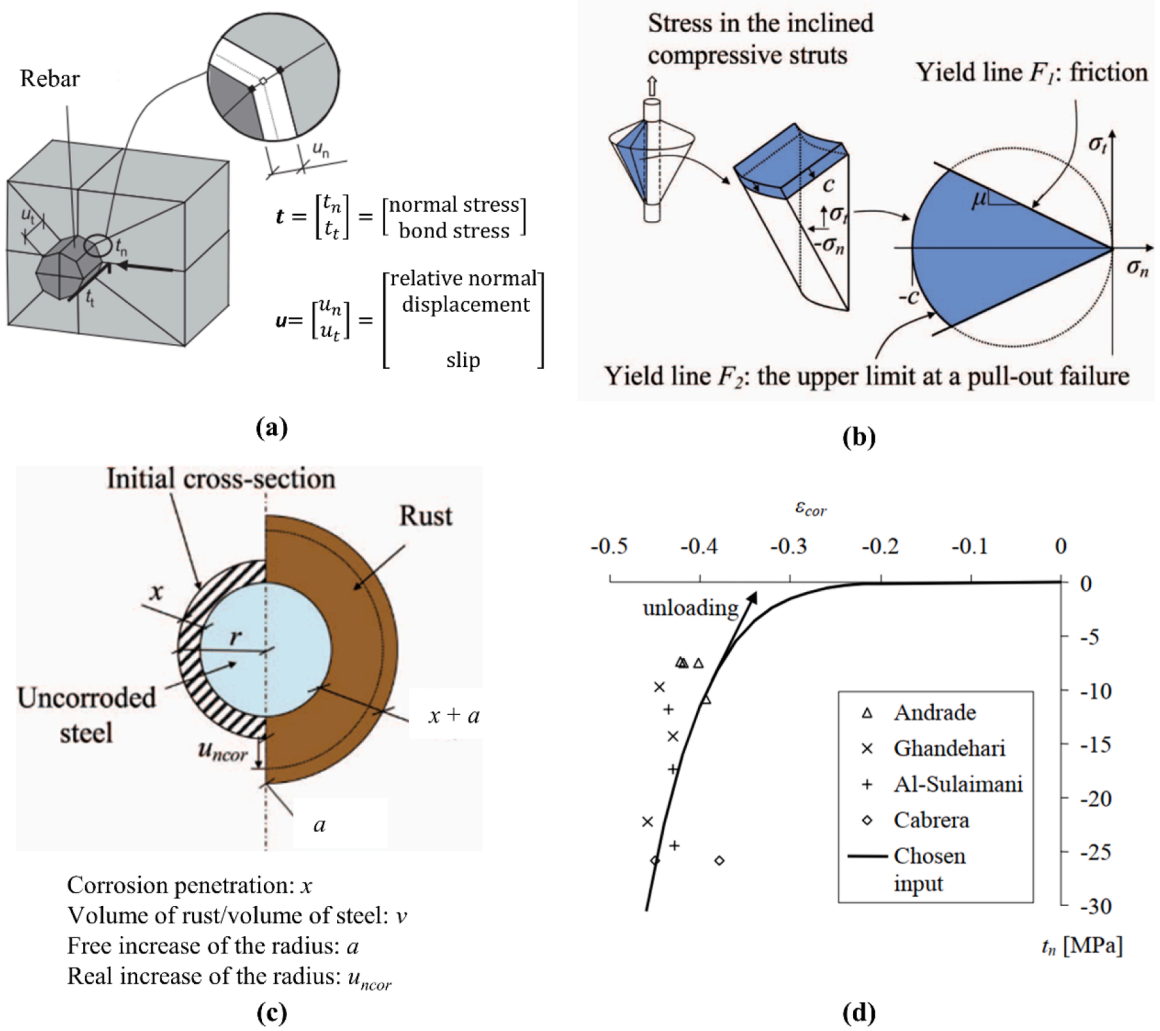

Fig. 2. Diagram of the bond-corrosion model: (a) physical interpretation of variables related to the interface; (b) yield surface of the bond model; (c) physical interpretation of the variables applied in the corrosion model; (d) assumed granular behaviour of the rust based on experimental data. Figures are modified based on [10,22,33,34].

elements. Geometric nonlinearity was considered. Displacement-controlled loading was first applied to the beam to generate bending cracks. The Newton-Raphson method was used for iteration with displacement and force norms used for convergence. Expansion of the interface elements representing corrosive products was induced by employing time steps. For each time step, the corrosion penetration upon each interface element was consistent. The Quasi-Newton method was applied with energy, displacement and force norms used for convergence. The finite element analyses were conducted by employing DIANA 10.5.

3. Assessment of the modelling method against experimental benchmarks

3.1. Overview of the experimental benchmarks

The modelling method was assessed in analyses of two RC beams from two different experimental campaigns [12,13]. Both beams were subjected to external loads to generate bending cracks. Thereafter, the beams were exposed to accelerated corrosion along a certain part of the bottom rebars, generating corrosion-induced cracks. Eventually, a combined pattern of bending and corrosion-induced cracks appeared. This is a proper representation of corrosion problems in RC beams in practice. Further, the cross-sectional loss was documented in detail with 3D scanning of the rebars after the corrosion phase.

The geometry and testing configurations are shown in Fig. 3. The first beam, labelled as SCB (RC beam with slightly corroded rebars) in this study, was tested by Berrocal et al. [12]. While subjected to sustained 4-point bending, the beam was exposed to accelerated corrosion with a constant current density of 75 $\mu A \cdot cm^{-2}$ for 49 days. This process resulted in the cross-sectional loss of 5 % and 10 % uniform and pitting corrosion, respectively. The central area on the front side of the beams was selected for Digital Image Correlation (DIC) observation. Crack widths and patterns were recorded.

The second beam, labelled as DN1 in the experimental campaign, was tested by Yang et al. [13]. Different from SCB, NaCl was added to the lower 50 mm of DN1 to shorten the corrosion initiation time. 3-point loading was first applied to the beam to generate pre-cracks; this load was thereafter removed. Next, accelerated corrosion with a constant current density of 220 $\mu A \cdot cm^{-2}$ was applied to the beam for 75 days causing cross-sectional loss of 16 % and 50 % uniform and pitting corrosion, respectively.

The model required a series of material properties as input. Detailed values and sources of these material properties are listed in Table 1. Most of the values were retrieved directly from the experimental records. Some values were calibrated based on Eurocode 2: Design of Concrete Structures [35] such as the tensile strength of concrete. For the weakened concrete, a multiplication factor of one minus the coefficient of variation (CoV) was applied to the material properties. Thus, the values of the weaker concrete were still within a realistic range. The values for the bond and corrosion models were taken from [33] and [22], respectively. The values for the corrosion rate were calibrated based on the experimental results. Corresponding to the earlier mentioned experimentally measured final corrosion levels, the corrosion penetration depths of pitting and uniform corrosion in SCB were 200 μm and 400 μm, respectively, while in DN1, they were 500 μm and 1800 μm, respectively. Accordingly, the corrosion rate of pitting and uniform corrosion in SCB were 1 μm per unit time and 2 μm per unit time, respectively, while in DN1, they were 1 μm per unit time and 3.6 μm per unit time, respectively. The total corroding time of SCB and DN1 were 200 unit time and 500 unit time, respectively. In such a manner, the corrosion penetration depth increased linearly with the time step. It is worth noting that in this study, corrosion was modelled as uniform around the bar. However, experimental observations indicated that the lower half of the rebar, particularly around bending cracks, experienced more corrosion than the upper part. For simplicity, this aspect was not incorporated into the models, as earlier analyses showed that corrosion on half of a bar resulted in approximately the same crack width as uniform corrosion [22]. Still, the same study showed that more localised corrosion pattern will influence the crack width. Future research incorporating realistic rebar geometries and varying corrosion around the bars could offer valuable insights.

3.2. Numerical results of the RC beam with slightly corroded rebars

Fig. 4 illustrates the crack pattern and width within the DIC monitoring area at the end of the corrosion process of the RC beam with slightly corroded rebars. Bending cracks are denoted as BC1 to BC8 in the figure for further discussion. Fig. 4a and b show visualisations of the crack pattern in the experiment and numerical analysis, respectively. For the experiment, a contour plot displaying DIC measurements is presented, while the numerical analysis includes a contour plot

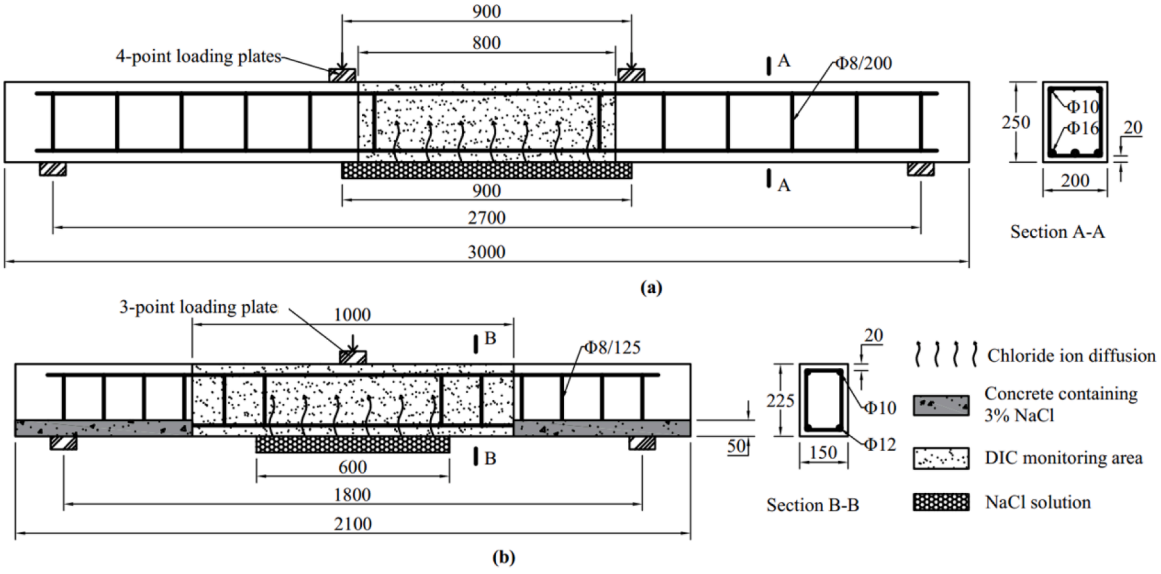

Fig. 3. Geometry and testing configurations of the modelled RC beams: (a) beam subjected to sustained loading during corrosion, with slightly corroded rebars (SCB) by Berrocal et al. [12]; (b) beam unloaded during corrosion, with severely corroded rebars (DN1) by Yang et al. [13].

Table 1
Material properties used in the model.

Material/Interface	Property/Parameter	SCB			DN1		
		Value	Unit	Source	Value	Unit	Source
Concrete	Elastic modulus E_c	36000	MPa	[35]	33000	MPa	[13]
	Poisson's ratio ν	0.2	-	[35]	0.2	-	[35]
	Tensile strength f_t	3.75	MPa	[35]	4.07	MPa	[35]
	Mode-I fracture energy G_f	0.115	N/mm	[36]	0.134	N/mm	[13]
	Compressive strength f_c	53.6	MPa	[12]	58	MPa	[13]
Weaker concrete	Elastic modulus $E_{c,\ weak}$	34000	MPa	Reduced based on CoV[a]	31000	MPa	Reduced based on CoV
	Poisson's ratio ν_{weak}	0.2	-	[35]	0.2	-	[35]
	Tensile strength f_t	3.54	MPa	Reduced based on CoV	3.84	MPa	Reduced based on CoV
	Mode-I fracture energy G_f	0.102	N/mm	Reduced based on CoV	0.119	N/mm	Reduced based on CoV
	Compressive strength $f_{c,\ weak}$	50.6	MPa	Reduced based on CoV	55	MPa	Reduced based on CoV
Steel	Elastic modulus *Es*	210000	MPa	[12]	191000	MPa	[13]
	Poisson's ratio ν	0.3	-	[12]	0.3	-	[13]
	Yield stress f_y	500	MPa	[12]	570	MPa	[13]
Corrosion product (interface)	Corrosion rate of pitting corrosion	1	μm/unit time	[12]	1	μm/unit time	[13]
	Corrosion rate of uniform corrosion	2	μm/unit time	[12]	3	μm/unit time	[13]
	Total corroding time	200	unit time	model	500	unit time	model
	Volume of the rust to the uncorroded steel, ν	2	-	[22]	2	-	[22]
	K_{cor}	7000	MPa	[22]	7000	MPa	[22]
	p	7	-	[22]	7	-	[22]

[a] For the weakened concrete, a multiplication factor of one minus the coefficient of variation (CoV) was applied.

depicting crack widths. Note that as a smeared crack model was used, the strains typically localise in one element row in the analysis. The longitudinal cracks that indicate corrosion-induced cracks appearing on the side surface of the beam are shown with black contour. Results show that the crack pattern exhibited a combination of bending and corrosion-induced cracks. The results indicated a good match between the crack patterns of the numerical model and the experiment. In both cases, longitudinal corrosion-induced cracks intersected with transversal bending cracks near the bottom rebar on the front surface of the beam. The maximum corrosion-induced cracks from numerical models and experiments were 0.58 mm and 0.56 mm, respectively. Additionally, corrosion-induced cracks were exclusively present on the side surfaces of the beam. Negligible corrosion-induced cracks were observed on the bottom surface of the beam, in both the numerical model and experiments.

The red dots in Fig. 4a, b represent the vertical width of the corrosion-induced cracks along the DIC monitoring area. Although the range of crack widths was similar in both the experiment and model (ranging from 0 to approximately 0.6 mm), the locations of maximum local crack widths could differ significantly. In the experiment, the maximum local crack width was primarily observed between the bending cracks, where uniform corrosion was assumed to occur. Conversely, in the numerical model, the maximum local cracks were mostly recorded at the positions of bending cracks, where pitting corrosion was expected to take place. This distinction is crucial for understanding the interaction between bending and corrosion-induced cracks, as it relates to identifying the most deteriorated section of the rebar and establishing the relationship between crack width and corrosion level. This difference will be further explored and investigated in Section 4.

Fig. 4c presents a 3D plot of the crack pattern obtained from the model. The left and right sections adjacent to the 3D plot depict crack patterns with and without bending cracks, respectively. A comparison of the crack patterns in individual sections reveals that corrosion-induced cracks propagated through the plane where the bottom rebar was located, while the presence of bending cracks did not affect the direction of propagation of the corrosion-induced cracks. Another observation from Fig. 4c is that the largest crack width appeared inside the concrete between the rebars. This phenomenon could not be observed in the experiments since the inspection of crack width inside the beam was not possible.

Fig. 5 illustrates the relationship between the crack width of corrosion-induced cracks and the corrosion level, represented as the ratio of the corroded area to the initial area of the rebar section. The distribution of uniform and pitting corrosion in the model aligned well with the experimental observations. However, it should be noted that the estimated corrosion level for uniform corrosion in the model was generally higher compared to the experiment. This is because the corrosion level as inputs in the model was an average of the 3D scanning results from three bottom bars, while the numerical results in this figure only pertained to the front rebar near the DIC monitoring area.

Additionally, Fig. 5 demonstrates that in the experiment, the locations of maximum local corrosion-induced crack widths did not coincide with areas of high local corrosion levels. For instance, the maximum local corrosion-induced crack between 1500 mm and 1800 mm was in the middle of the pits rather than overlapping with them. As discussed in Section 2, the position of the bending crack indicates the location of pitting corrosion on the rebar. This implies that, according to the experiment, the most severe corrosion level cannot be determined solely by examining the largest corrosion-induced crack width on the beam surface. Furthermore, the corrosion level of pits cannot be precisely predicted based on the bending crack width either. Fig. 6 provides an example where similar bending crack widths (BC3, 5–8) correspond to corrosion levels variating significantly from 5 % to 13 %. In contrast, according to the numerical results, the largest corrosion level mostly corresponded to the largest corrosion-induced cracks, suggesting that the crack width on the beam surface can be used to determine the corrosion level.

These inconsistencies between the experimental and numerical results can be explained by the following hypotheses. In the experiment, the rapid accelerated corrosion process generates soluble corrosion products, and the opening of bending cracks provides paths for transporting the corrosion products away from the rebar. Therefore, the corrosion products will not accumulate around the rebar near the

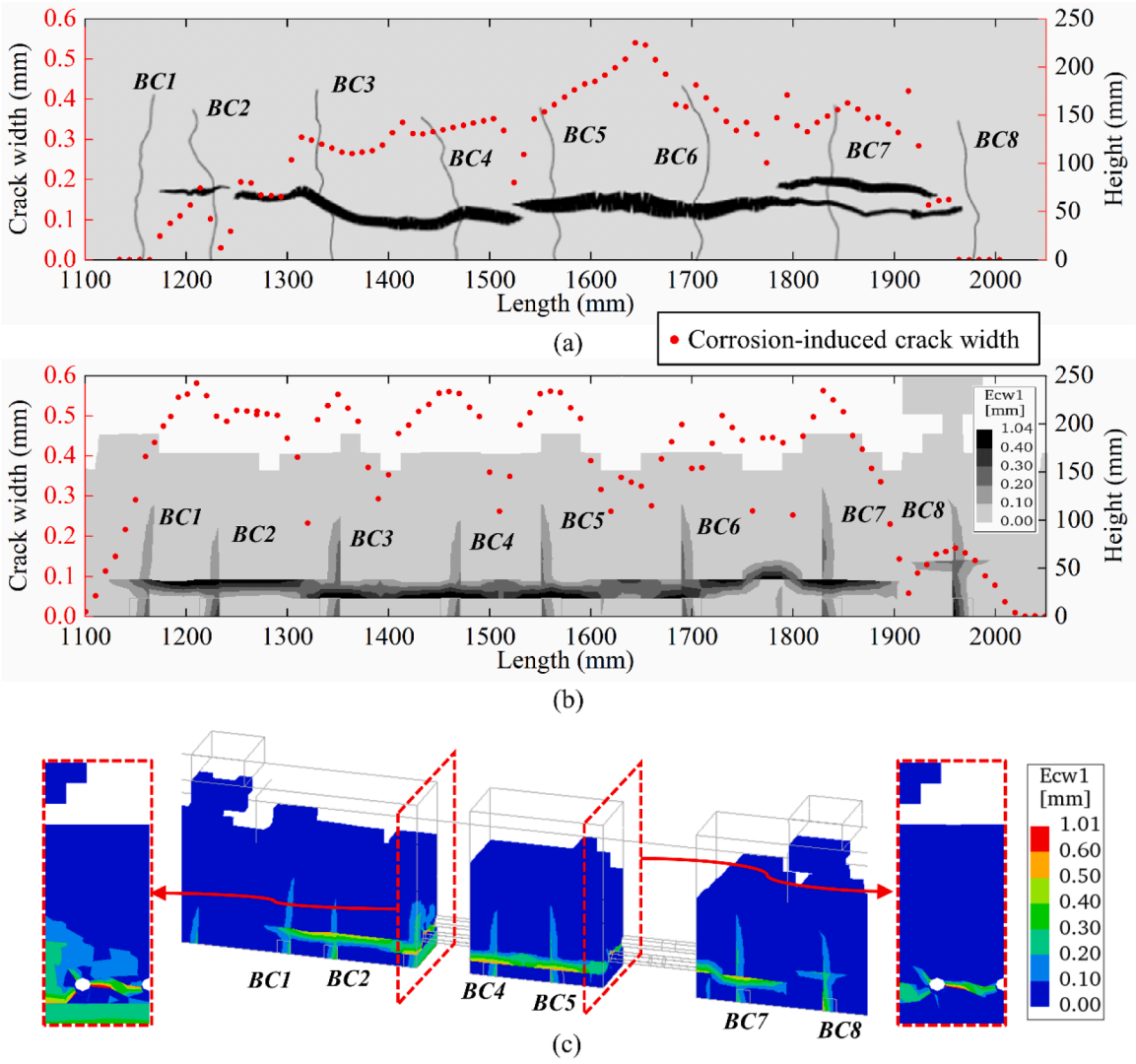

Fig. 4. Crack patterns of combined bending and corrosion-induced cracks on the side surface of the beam at the end of (a) experiment and (b) numerical analysis. Cracks are marked by black contour. The crack width of the corrosion-induced cracks is indicated by red dots; (c) 3D plot of the crack pattern in the model. In all figures, BCx represents the label of bending cracks. Ecw1: principal crack width.

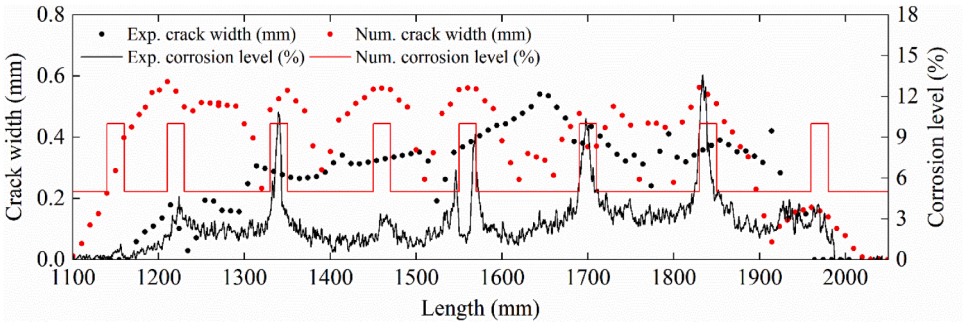

Fig. 5. Crack width of the corrosion-induced cracks, together with the corrosion level of the bottom rebar from both the experimental and numerical results, at the end of the experiment/analysis.

bending cracks. The stresses are thus released, and no corrosion-induced cracks will form. Conversely, the corrosion products between two bending cracks are well sealed by the surrounding concrete. This results in the generation of hoop tensile stresses in the surrounding concrete, leading to the initiation of corrosion-induced cracks amid bending cracks. However, in the numerical models, the transport was not included, and the corrosion rate of the pitting corrosion was set higher than that of the uniform corrosion. This generates substantial deformation in the interface elements at the pits and the potential generation of increased normal stresses. Consequently, corrosion-induced cracks initiate from the vicinity of bending cracks in the analysis instead of the midpoint between them, as was noted in the experiment.

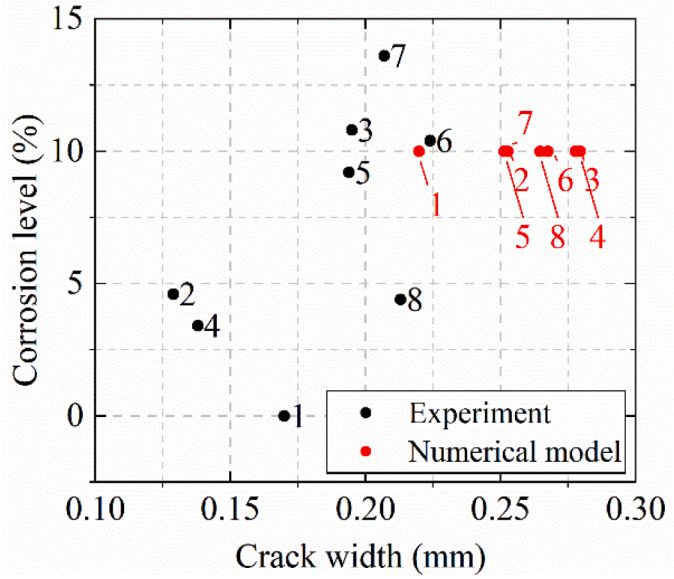

Fig. 6. Crack width of the bending cracks and the corresponding corrosion level of the rebar. Number 1–8 corresponds to BC1- BC8 in Fig. 4.

The evolution of crack patterns is compared between experimental observations and the numerical model (Fig. 7). In the experiments, corrosion-induced cracks were observed to initiate between bending cracks (top graphics in Fig. 7b, c, and d) and subsequently propagated towards adjacent bending cracks, connecting with other corrosion-induced cracks to form longitudinal cracks on the beam surface (top graphics in Fig. 7e, f). In contrast, the numerical model showed that corrosion-induced cracks initiated at the intersections with bending cracks (bottom graphics in Fig. 7b, c, and d) before connecting with neighbouring cracks (bottom graphics in Fig. 7e, f).

Fig. 8 presents the evolution of crack width of the corrosion-induced cracks in the vertical direction at multiple locations on the front surface of the beam. The experimental procedure involved applying accelerated corrosion for 5 weeks, followed by 2 weeks without corrosion, and then another 2 weeks of corrosion. It is important to note that during the intermediate period without corrosion, the crack width remained approximately constant. Therefore, this intermediate period is concealed in the figure to highlight the relationship between corrosion-induced crack width and time subjected to non-stop corrosion.

The results displayed in Fig. 8 demonstrate that both the experimental and numerical models indicated an approximately linear correlation between corrosion-induced crack width and time after the initiation of cracks, whether it was near the pits (BC4, BC5) or between the pits (CC1, CC2). Since the impressed current remains constant, it can be assumed that the local corrosion rate remains approximately constant over time. Consequently, at a specific location along the rebar, the rate of change in corrosion-induced crack width can be considered proportional to the rate of change in corrosion level.

3.3. Numerical results of the RC beam with severely corroded rebars

Fig. 9 presents a comparison between the experimental and numerical results of beam DN1, whose rebars were severely corroded. It is important to highlight that due to the higher current density (220 $\mu A \cdot cm^{-2}$) and extensive corrosion of the rebar within this beam, the distribution of corrosion appeared to be more uniform in comparison to that of SCB (subjected to a lower current density of 75 $\mu A \cdot cm^{-2}$). Consequently, the differentiation between pitting and uniform corrosion can pose challenges. To determine the specific locations of predetermined pits in the analysis, these pits are assumed to coincide with the positions of bending cracks. The crack pattern observed in the numerical model aligned well with that of the experiment. Both the experiment and the numerical model demonstrate that corrosion-induced cracks occurred exclusively on the bottom surface of the beam. The maximum corrosion-induced cracks from numerical models and experiments were 1.21 mm and 1.43 mm, respectively. This can be attributed to the wider spacing between the rebars compared to the RC beam with slightly corroded rebars (SCB). Consequently, the initiation of corrosion-induced cracks did not take place between the rebars but rather propagated towards the bottom surface of the beam.

To evaluate the extent of corrosion-induced cracking, the crack widths were measured at intervals of 150 mm along the bottom of the beam in the experiment. Comparing the corresponding corrosion levels

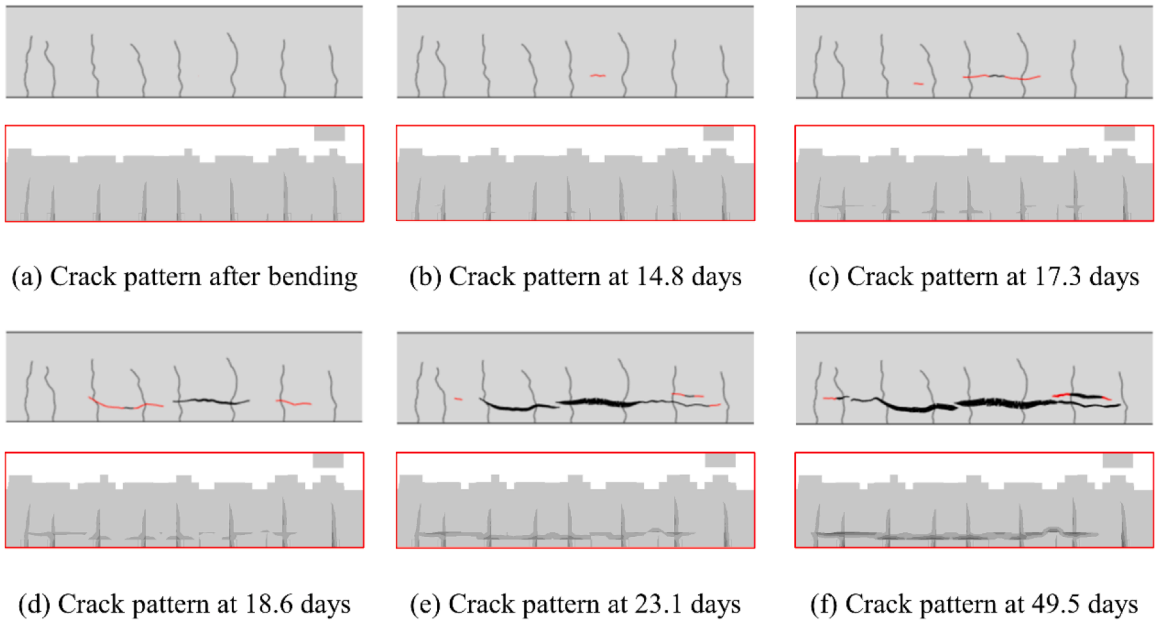

Fig. 7. Evolution of crack patterns from experimental and numerical results with a focus on the central part of the beam (from 1100 mm to 2100 mm). In each subfigure, the top and bottom show experimental and numerical results, respectively. In each new stage of the experiment, newly appeared corrosion-induced cracks are marked in red.

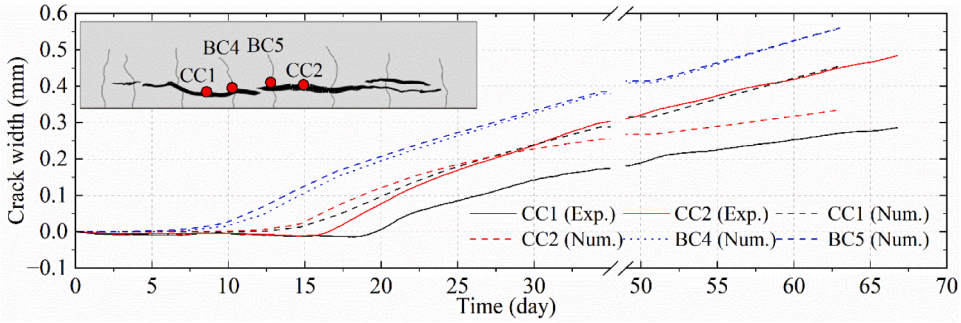

Fig. 8. Crack width evolution of selected positions along the corrosion-induced cracks. CCx represents positions upon corrosion-induced cracks. BCx represents positions upon the intersections between bending and corrosion-induced cracks.

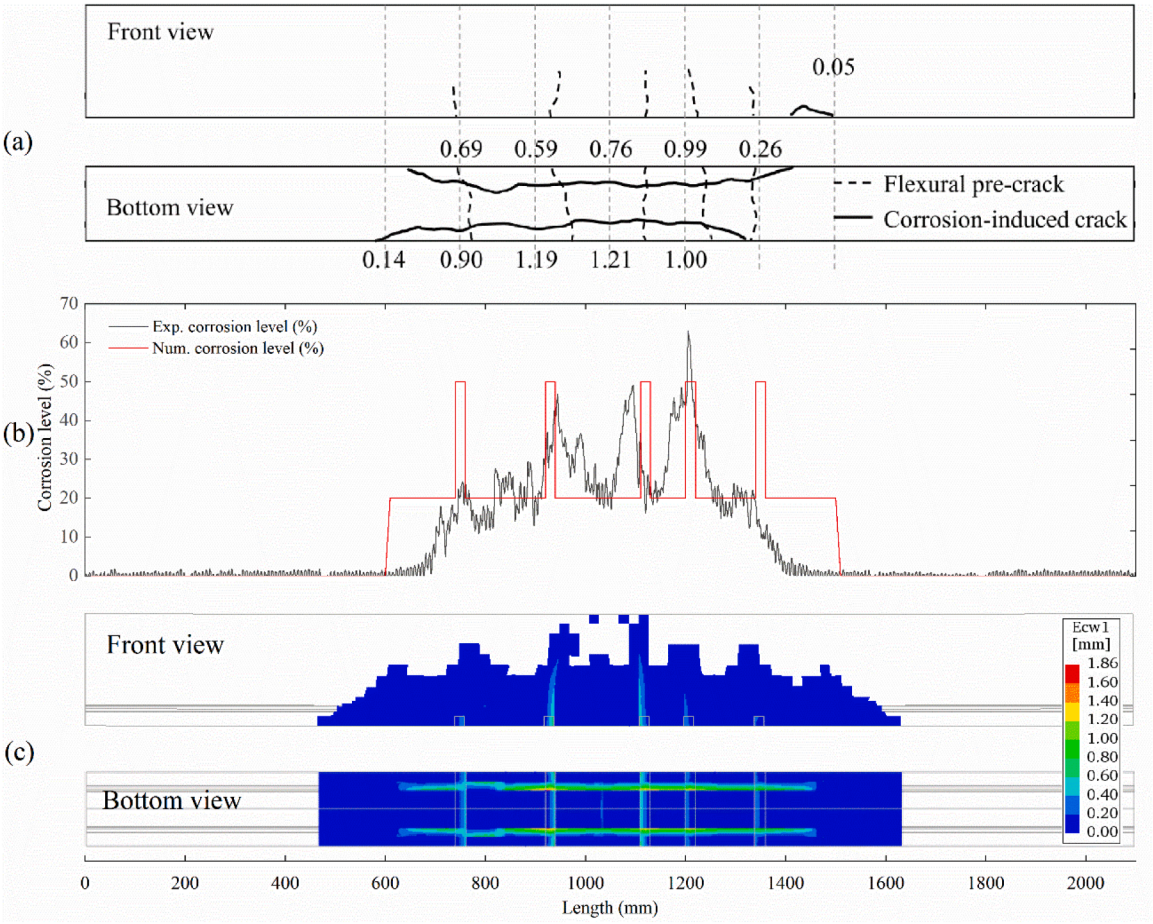

Fig. 9. Crack pattern, width, and corrosion level of DN1. (a) and (c): Crack pattern and width on the front and bottom surfaces at the end of the experiment and numerical analysis, respectively. The corrosion-induced crack widths (unit in mm) marked in (a) are measured every 150 mm. (b) Crack width of the corrosion-induced cracks on the bottom surface corresponding to the corrosion level of the bottom rebar. Ecw1: principal crack width.

at the rebar, as depicted in Fig. 9, reveals that crack width alone cannot determine the highest corrosion level along the rebar. For instance, crack widths of 1.21 mm and 1.00 mm corresponded to local corrosion levels of 40 % and 62 % respectively. Conversely, in the numerical model, the location of the largest crack width coincided with the position of the highest corrosion level, specifically that of pitting corrosion. This suggests that the observations made in Section 3.2, which applied to the RC beam with severely corroded rebars, remain valid. Furthermore, despite variations in current density, both DN1 and SCB exhibited similar crack patterns involving transverse bending and longitudinal corrosion-induced cracks.

It is important to note that the experimental benchmarks in this study were established through accelerated testing techniques, involving electric current to induce corrosion in the steel reinforcement. Several uncertainties regarding how well accelerated methods mimic natural corrosion exist, e.g., regarding the corrosion morphology [37], and the solubility [38] of the corrosion products. With more soluble corrosion products in accelerated corrosion [26,38], a larger effect of transport of corrosion products is expected for accelerated corrosion than for natural corrosion. To further apply this modelling method to beams with naturally corroded steel reinforcement, more experimental data regarding natural corrosion is required to enable calibration and validation.

4. Interaction between bending and corrosion-induced cracks

The present study employs the established modelling method to investigate the intersection between bending and corrosion-induced cracks. A parametric study was conducted, focusing on three significant factors: the transport of corrosion products, the spacing between bending cracks, and the width of the bending cracks. Fig. 10 depicts a representative configuration used in the analysis, featuring a beam with dimensions of 1000 × 160 × 200 mm^3 (length × depth × height). To facilitate the parametric study, the front half of the beam was symmetrically modelled. By employing smaller dimensions of the beam compared to the experimental counterparts, greater control over the positioning and number of bending cracks was achieved. Moreover, a refined mesh size of 10 mm was utilised, enabling more precise observation of crack propagation. The beam was subjected to four-point bending to generate bending cracks. The material properties followed the ones of DN1 in Section 3. The width of the pits was set as 20 mm.

4.1. Influence of transport of corrosion products via simplified approach

As discussed in Section 3, the reasons behind some disparities between the numerical model and experimental observations regarding the initiation and evolution of corrosion-induced cracks remained unclear. Berrocal et al. [12] hypothesised that with the experimental configurations (namely, the beams were subjected to accelerated corrosion and the bending cracks were kept open), the soluble corrosion products could be transported through the bending cracks towards the beam surface. Therefore, the corrosion products did not accumulate around the rebar near the bending cracks. The stresses would thus be released, and no corrosion-induced cracks would form. Conversely, the corrosion products in the middle of uniform corrosion, between two bending cracks, were well sealed by the surrounding concrete. This resulted in the generation of hoop tensile stresses in the surrounding concrete, leading to the initiation of corrosion-induced cracks [12]. However, these deductions are still unverified by experimental evidence.

In this section, a simplified approach to account for transport of corrosion products through cracks was applied. The corrosion rate was decreased to only consider expansion of corrosion products applying pressure to the concrete, thus not including corrosion products being transported away through cracks. Consequently, a corrosion rate of 0 corresponds to all corrosion products being transported away from the rebar, without applying any normal stress. It should be noted that even though this simplification indirectly represents the mechanical behaviour of corrosion products affected by their transport near the bending cracks, the physical behaviour of the transport of corrosion products was not modelled.

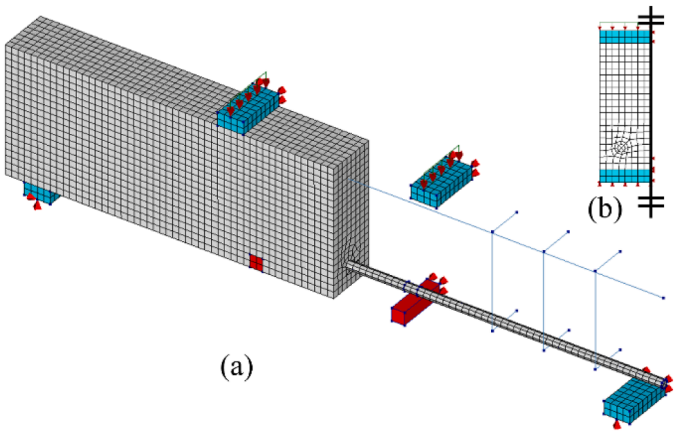

Fig. 10. Model for the parametric study. (a) The meshed model. The right half of the concrete is hidden to expose the rebar. (b) The right elevation of the symmetric model.

Fig. 11 illustrates the corrosion rates of pitting and uniform corrosion in four cases examined in this parametric study. For the uniform corrosion in all cases, the corrosion rate was set to 1 μm per unit time. In Cases, A, B, and C, the corrosion rates of pitting corrosion were set to 3, 1, and 0 μm per unit time, respectively. In Case D, the length affected by transport through the bending cracks was assigned a value of 60 mm and a corrosion rate of 0 μm per unit of time. This setting simulates the scenario where corrosion products in a wider range close to the bending cracks are transported away from the rebar.

Fig. 12 illustrates the initiation and final crack patterns resulting from corrosion in all cases. In the figure, the initiating positions of corrosion-induced cracks are marked with red dashed circles. Note that as the corrosion-induced cracks initiated, some vertical cracks paralleling the bending cracks appeared at the same position. In cases A, B, and C, the corrosion-induced cracks originated from the locations of bending cracks, and ultimately, fully developed between the two bending cracks on the bottom surface. In contrast, Case D exhibited different behaviour, where the expansion of corrosion products initially triggered horizontal corrosion-induced cracks between them accompanied by vertical cracks at the same location. Additionally, the corrosion-induced cracks between bending cracks fully developed on the front surface of the beam. Comparing cases, A, B, and C reveals that simply reducing the corrosion rate of interface elements at the pits, which represented increasing transport of corrosion products, did not alter the initiation position of corrosion-induced cracks. This indicates that if the range affected by transport through the bending cracks remains the same length as pits determined from the experiments, merely increasing the transport of pitting corrosion may not alter the stress concentration state to the uniform corrosion between the bending cracks. Consequently, corrosion-induced cracks will continue to initiate at the intersection with the bending cracks. In contrast, as the range affected by transport through the bending cracks was increased as in Case D, tensile stresses in the concrete concentrated between the bending cracks, leading to the initiation of corrosion-induced cracks at these positions.

To further assess the previous discussion, the radial expansion of the interface elements in all cases is examined at the initiation of corrosion-

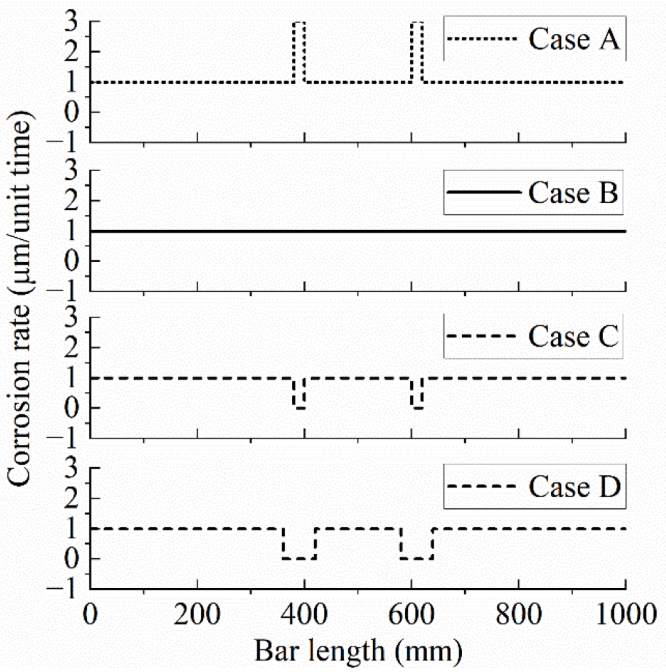

Fig. 11. Corrosion rates of pitting and uniform corrosion along the bar in Cases A-D.

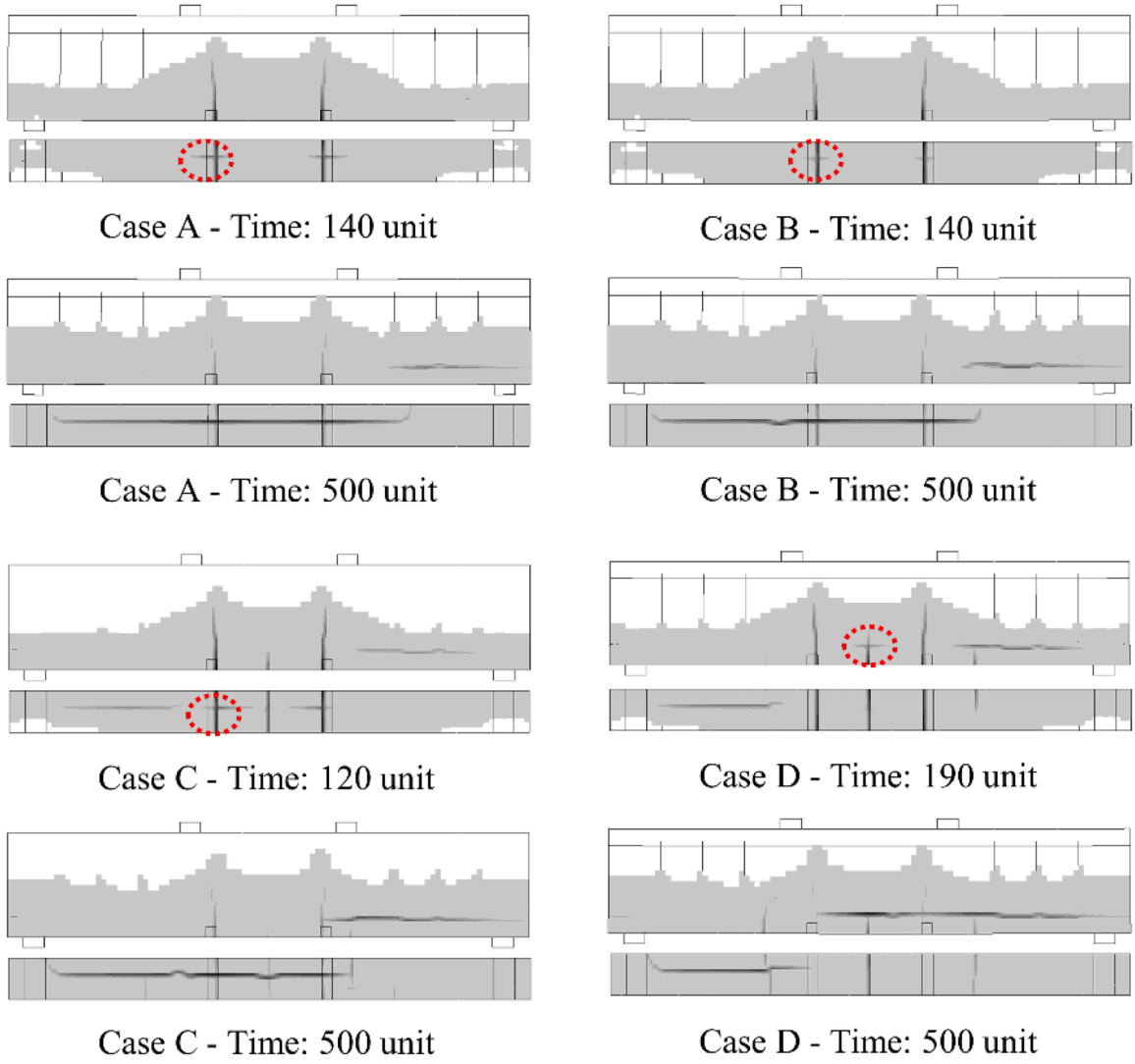

Fig. 12. Initiation of corrosion-induced cracks and final crack patterns of cases A-D. In each subfigure, both the front and bottom views of the beam are presented. The red-dotted circle indicates the starting locations of the corrosion-induced cracks.

induced cracks, as depicted in Fig. 13. In cases A and B, where the corrosion rates of pits were set to 3 and 1 μm per unit time, respectively, the interface elements exhibited the highest expansion precisely at the pits. On the other hand, in Case C, despite setting the expansion of pits to zero, the expansion of the interface elements still reached its peak near the pits (i.e., near the bending cracks). In Case D, however, the highest expansion of the interface elements was observed in the middle region between the bending cracks, indicating the initiation of corrosion-induced cracks at this location. Thus, the initiation of corrosion-induced cracks shifts towards the middle region when the transport of corrosion products takes place in a wide region near the bending cracks. Moreover, this finding underscores that the transport of corrosion products plays a crucial role in the interaction between bending and corrosion-induced cracks. However, it is worth noting that this numerical study was based on accelerated-corrosion experiments. In the natural environment, corrosion of rebars takes place at an extremely low rate [18,39,40]. The transport of corrosion products can be obstructed thus resulting in high normal stresses in surrounding concrete. Therefore, the settings of the models in this study may need to be adjusted and generated, and the observations and conclusions remain to be further verified.

The corrosion-induced crack width for all cases is presented in Fig. 14. It should be noted that if corrosion-induced cracks are observed on both the front and bottom surfaces, the larger crack width is selected for analysis. Upon comparing cases A, B, and C, a general trend emerged where the crack width was the highest at the pits (i.e., at the bending cracks) and decreased towards the middle region located between the bending cracks. Conversely, in Case D, the crack width was the highest in the middle region between the bending cracks and decreased towards the neighbouring bending cracks. Notably, the crack width distribution in Case D closely resembled the experimental results shown in Fig. 5. This finding suggests a high possibility that, in the realistic scenario, the corrosion products near the bending cracks may be transported in a range wider than the determined pit length in the experiments.

4.2. *Influence of the distance between bending cracks*

This section investigates the influence of the distance between bending cracks on the interaction with corrosion-induced cracks. This was achieved by modifying the distance between weakened elements. Fig. 15a illustrates three different distances between bending cracks implemented in the model: 220 mm, 150 mm, and 100 mm, representing 2, 3, and 4 pre-set bending cracks in the central part of the beam, respectively. The settings for the corrosion rates along the rebars were set the same as those of Case D in Section 4.1. It is important to note that the applied bending loads responsible for generating the bending cracks

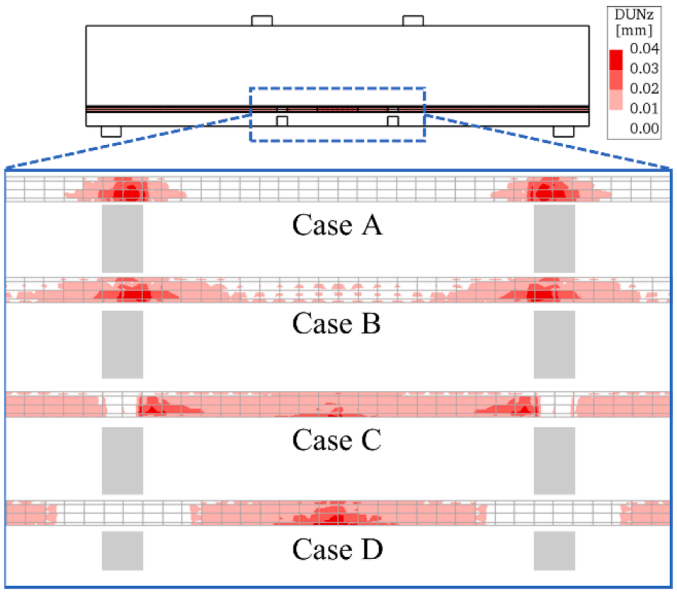

Fig. 13. Radial expansion of the interface elements during the onset of corrosion-induced cracks. The grey-striped areas indicate the ranges and locations of the bending cracks. DUNz: relative normal displacement.

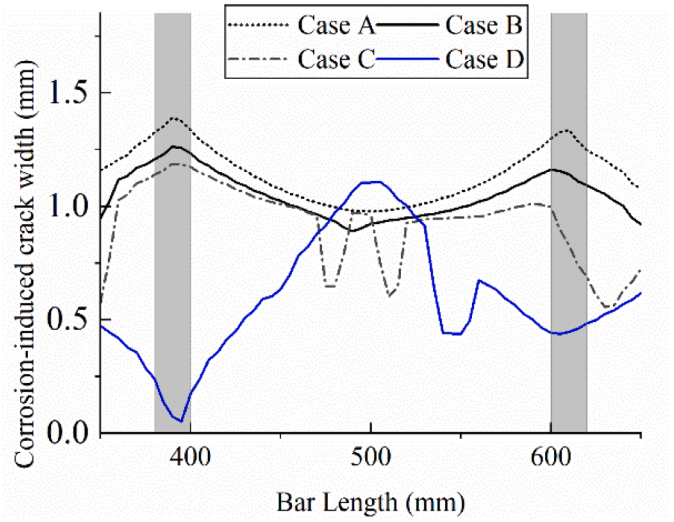

Fig. 14. Corrosion-induced crack widths of cases A-D at the end of the analysis. The grey-striped areas indicate the position of bending cracks.

remain consistent across all cases.

Fig. 15b illustrates the crack patterns observed in beams with varying distances between bending cracks at the onset of corrosion-induced cracks. In the figure, the initiating positions of corrosion-induced cracks are marked with red dashed circles. Note that as the corrosion-induced cracks initiated, some vertical cracks paralleling the bending cracks appeared at the same position. The results demonstrate that when the distance between bending cracks decreased from 220 mm to 150 mm, corrosion-induced cracks continued to initiate between the bending cracks. However, upon a further reduction of the distance to 100 mm, corrosion-induced cracks initiated at the intersection with the bending cracks instead of at the midpoint between the bending cracks.

4.3. Influence of the bending crack width

This section investigates the impact of bending crack width on its interaction with corrosion-induced cracks. For reference, Case D from Section 4.1 was selected. To generate varying bending crack widths on the bottom surface of the beam, different bending loads were applied. Three cases were examined, with bending crack widths of 0.25 mm (Case D), 0.49 mm, and 0.64 mm, respectively.

The crack patterns at the initiation of corrosion-induced cracks is depicted in Fig. 16. In the figure, the initiating positions of corrosion-induced cracks are marked with red dashed circles. Note that as the corrosion-induced cracks initiated, some vertical cracks paralleling the bending cracks appeared at the same position. The figure demonstrates that as the bending crack width increased, the position where corrosion-induced cracks initiated remained consistent, specifically between the bending cracks. The distribution of corrosion-induced crack widths is further illustrated in Fig. 17. The results indicate that as the bending crack width increased, the width of corrosion-induced cracks decreased, although the largest crack width was still observed in the central part between the bending cracks. As the bending crack width increased from 0.25 mm to 0.64 mm, the largest corrosion-induced crack width decreased from 1.16 mm to 0.61 mm. Another interesting finding is that larger bending crack width produced less varied corrosion-induced cracks along the rebar.

5. Conclusions

In this study, a comprehensive 3D finite element modelling method was developed to examine the interaction between bending and corrosion-induced cracks in reinforced concrete (RC) beams. The approach encompasses several notable features: it effectively considers the bending action accompanied by the expansion of corrosion products; it establishes a connection between bending cracks and pitting corrosion; and in a simplified manner it considers the effect of corrosion products being transported through bending cracks. To ensure the reliability of the model, assessments were performed using a beam with slightly corroded rebars and another with severely corroded rebars, both sourced from experimental campaigns. Subsequently, the method was employed in a parametric study to explore the influence of crucial factors on the interaction between bending and corrosion-induced cracks. The significant findings derived from this study are summarised as follows.

The 3D modelling method demonstrated its capability to accurately simulate the behaviour of RC beams subjected to bending action accompanied by corrosion. The models provided reasonable representations of crack patterns and the time history of crack widths against the experimental evidence, both for RC beams with slightly and severely corroded rebars. Specifically, for the beam with slightly corroded reinforcement, maximum corrosion-induced cracks from numerical models and experiments were 0.58 mm and 0.56 mm, respectively. For the beam with severely corroded reinforcement, the corresponding values were 1.21 mm and 1.43 mm. Moreover, the method offered the advantage of visualising the internal state of the beams, including the propagation of internal cracks and the expansion of corrosion products represented by the interface elements.

The modelling results revealed that the transport of corrosion products played a decisive role in the initiation and evolution of corrosion-induced cracks. Specifically, when the transport of corrosion was assumed to influence a wide region near bending cracks, corrosion-induced cracks occurred amidst the bending cracks. Conversely, corrosion-induced cracks initiated from the position of bending cracks, and the largest crack width occurred at the intersection with bending cracks when no transport of corrosion products was assumed to take place. The evolution and width of corrosion-induced cracks observed in the former case aligned with experimental observations. These findings suggest that the most heavily corroded area of the steel reinforcement is not directly correlated with the initiation of corrosion-induced cracks or the widest crack width. With the demand of detecting the most corroded area via visual inspection of combined bending and corrosion-induced cracks, it is essential to consider the three-dimensional effects and the

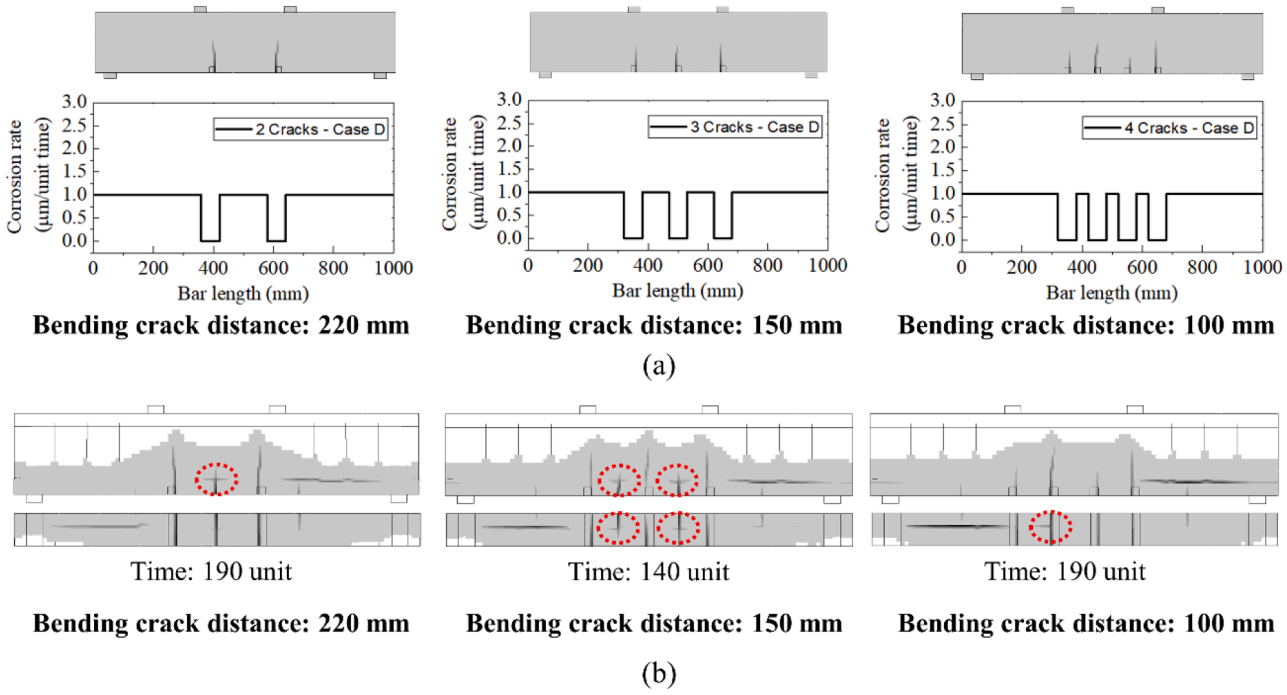

Fig. 15. (a) Cases for studying the influence of the distance between bending cracks on their interaction with corrosion-induced cracks. (b) Crack patterns of beams with different distances of bending cracks at the onset of corrosion-induced cracks. In each subfigure, both the front and bottom views of the beam are presented. The red-dotted circle indicates the starting locations of the corrosion-induced cracks.

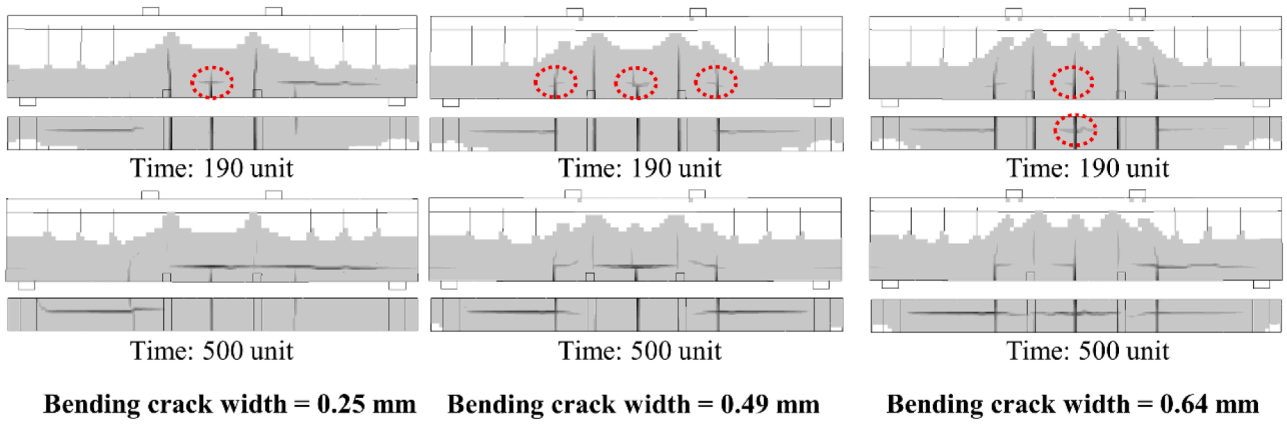

Fig. 16. Crack patterns of beams based on Case D with different bending crack widths. In each subfigure, both the front and bottom views of the beam are presented. The red-dotted circle indicates the starting locations of the corrosion-induced cracks.

transport of the corrosion products.

The analyses predicted that as the distance between bending cracks decreased from 220 mm to 150 mm, corrosion-induced cracks continued to initiate between the bending cracks. However, upon a further reduction of the distance to 100 mm, corrosion-induced cracks initiated at the intersection with the bending cracks instead of at the midpoint between the bending cracks.

Furthermore, the analyses predicted that by increasing the bending crack width, the evolution and initiation of corrosion-induced cracks remained consistent. However, the corrosion-induced crack width along the rebar generally decreased as the bending crack width increased. Additionally, larger bending crack width produced less varied corrosion-induced cracks along the rebar.

In conclusion, the 3D modelling method developed in this research offers a reasonable simulation of the behaviour exhibited by RC beams under the influence of bending and corrosion. The findings underscore the significance of considering the three-dimensional effects and the transport of corrosion products when investigating the initiation and progression of cracks induced by bending action accompanied by corrosion. These insights enhance the understanding of the complex interaction between bending and corrosion effects in RC beams. Moreover, it is worth noting that the modelling method in this study relies on RC beams whose steel reinforcement underwent accelerated corrosion. To further apply this modelling method to beams with naturally corroded steel reinforcement, more experimental data regarding natural corrosion is required to enable calibration and validation.

CRediT authorship contribution statement

Lang-Zi Chang: Conceptualisation, Methodology, Formal analysis, Writing – original draft, Visualisation. **Jonathan Thorsson:** Conceptualisation, Methodology, Formal analysis, Writing – review & editing. **Karin Lundgren:** Conceptualisation, Methodology, Writing - review & editing, Supervision, Project administration, Funding

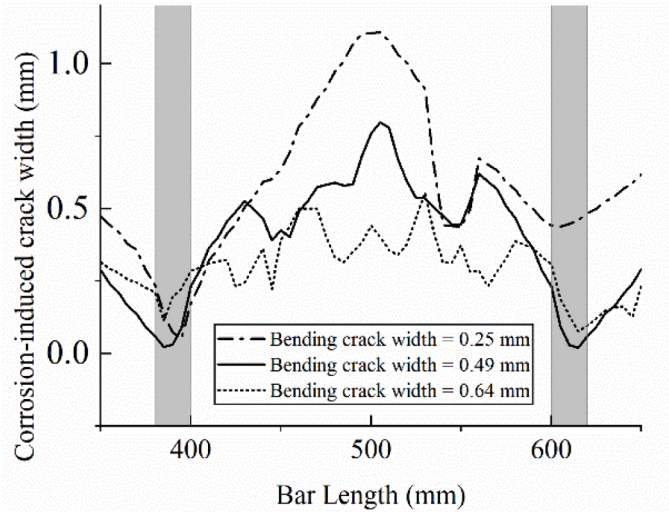

Fig. 17. Corrosion-induced crack widths of beams with different bending crack widths. The grey-striped areas indicate the position of bending cracks.

acquisition.

Declaration of Competing Interest

The authors declare that they have no known competing financial interests or personal relationships that could have appeared to influence the work reported in this paper.

Data availability

Data will be made available on request.

Acknowledgements

This work was financially supported by the Swedish Transport Administration (grant no. 2021/27819) and the Swedish Research Council Formas (grant no. 2019-00497). The computations were performed on resources at the Chalmers Centre for Computational Science and Engineering (C3SE) provided by the Swedish National Infrastructure for Computing (SNIC). Special thanks go to Dr. Carlos Gil Berrocal, Associate Prof. Ignasi Fernandez and Dr. Jincheng Yang for providing original experimental data.

References

[1] X. Wang, M.N. Nguyen, M.G. Stewart, M. Syme, Analysis of Climate Change Impacts on the Deterioration of Concrete Infrastructure – Part 1: Mechanisms, Practices, Modelling and Simulations, CSIRO Climate Adaptation Flagship, 2010.
[2] S.W. Tang, Y. Yao, C. Andrade, Z.J. Li, Recent durability studies on concrete structure, Cem. Concr. Res. 78 (2015) 143–154.
[3] H. Zhao, Y. Hu, Z. Tang, K. Wang, Y. Li, W. Li, Deterioration of concrete under coupled aggressive actions associated with load, temperature and chemical attacks: A comprehensive review, Constr. Build. Mater. 322 (2022).
[4] C.-p Gu, G. Ye, W. Sun, A review of the chloride transport properties of cracked concrete: experiments and simulations, J. Zhejiang Univ. -Sci. A 16 (2) (2015) 81–92.
[5] Y. Zheng, Y. Zhou, Y. Zhou, T. Pan, L. Sun, D. Liu, Localized corrosion induced damage monitoring of large-scale RC piles using acoustic emission technique in the marine environment, Constr. Build. Mater. 243 (2020).
[6] W. Zhu, R. François, Corrosion of the reinforcement and its influence on the residual structural performance of a 26-year-old corroded RC beam, Constr. Build. Mater. 51 (2014) 461–472.
[7] S. Coccia, S. Imperatore, Z. Rinaldi, Influence of corrosion on the bond strength of steel rebars in concrete, Mater. Struct. 49 (1–2) (2014) 537–551.
[8] D. Coronelli, P. Gambarova, Structural assessment of corroded reinforced concrete beams: modeling guidelines, J. Struct. Eng. 130 (8) (2004) 1214–1224.
[9] D.V. Val, Deterioration of strength of RC beams due to corrosion and its influence on beam reliability, J. Struct. Eng. 133 (9) (2007) 1297–1306.
[10] K. Zandi Hanjari, K. Lundgren, M. Plos, D. Coronelli, Three-dimensional modelling of structural effects of corroding steel reinforcement in concrete, Struct. Infrastruct. Eng. 9 (7) (2013) 702–718.
[11] Y. Zheng, Y. Zhou, Y. Zhou, T. Pan, Q. Zhang, D. Liu, Cracking behavior of reinforced concrete beams strengthened with CFRP anchorage system under cyclic and monotonic loading, Eng. Struct. 207 (2020).
[12] C.G. Berrocal, I. Fernandez, R. Rempling, The interplay between corrosion and cracks in reinforced concrete beams with non-uniform reinforcement corrosion, Mater. Struct. 55 (4) (2022).
[13] J. Yang, R. Haghani, T. Blanksvärd, K. Lundgren, Experimental study of FRP-strengthened concrete beams with corroded reinforcement, Constr. Build. Mater. 301 (2021).
[14] A.S. Al-Harthy, M.G. Stewart, J. Mullard, Concrete cover cracking caused by steel reinforcement corrosion, Mag. Concr. Res. 63 (9) (2011) 655–667.
[15] C. Andrade, C. Alonso, F.J. Molina, Cover cracking as a function of bar corrosion: Part I-experimental test, Mater. Struct. 26 (8) (1993) 453–464.
[16] J. Rodriguez, L.M. Ortega, J. Casal, Load carrying capacity of concrete structures with corroded reinforcement, Constr. Build. Mater. 11 (4) (1997) 239–248.
[17] T. Vidal, A. Castel, R. François, Analyzing crack width to predict corrosion in reinforced concrete, Cem. Concr. Res. 34 (1) (2004) 165–174.
[18] L. Yu, R. François, V.H. Dang, V. L'Hostis, R. Gagné, Distribution of corrosion and pitting factor of steel in corroded RC beams, Constr. Build. Mater. 95 (2015) 384–392.
[19] F.J. Molina, C. Alonso, C. Andrade, Cover cracking as a function of rebar corrosion: Part 2—numerical model, Mater. Struct. 26 (9) (1993) 532–548.
[20] A. Michel, B.J. Pease, A. Peterová, M.R. Geiker, H. Stang, A.E.A. Thybo, Penetration of corrosion products and corrosion-induced cracking in reinforced cementitious materials: experimental investigations and numerical simulations, Cem. Concr. Compos. 47 (2014) 75–86.
[21] C. Fahy, S.J. Wheeler, D. Gallipoli, P. Grassl, Corrosion induced cracking modelled by a coupled transport-structural approach, Cem. Concr. Res. 94 (2017) 24–35.
[22] K. Lundgren, Bond between ribbed bars and concrete. Part 2: the effect of corrosion, Mag. Concr. Res. 57 (7) (2005).
[23] Y.Z. Wang, Y.X. Zhao, F.Y. Gong, J.F. Dong, K. Maekawa, Developing a three-dimensional finite element analysis approach to simulate corrosion-induced concrete cracking in reinforced concrete beams, Eng. Struct. 257 (2022).
[24] P. Koteš, M. Brodňan, J. Vaňrek, Determination of corrosion of the steel reinforcement and application to a bridge structure. Maintenance, Monitoring, Safety, Risk and Resilience of Bridges and Bridge Networks, CRC Press, 2016, 485-485.
[25] E. Chen, C.G. Berrocal, I. Löfgren, K. Lundgren, Comparison of the service life, life-cycle costs and assessment of hybrid and traditional reinforced concrete through a case study of bridge edge beams in Sweden, Struct. Infrastruct. Eng. 19 (1) (2021) 39–57.
[26] C.G. Berrocal, I. Fernandez, K. Lundgren, I. Löfgren, Corrosion-induced cracking and bond behaviour of corroded reinforcement bars in SFRC, Compos. Part B: Eng. 113 (2017) 123–137.
[27] M. Tahershamsi, I. Fernandez, K. Zandi, K. Lundgren, Four levels to assess anchorage capacity of corroded reinforcement in concrete, Eng. Struct. 147 (2017) 434–447.
[28] J. Ožbolt, G. Balabanić, G. Periškić, M. Kušter, Modelling the effect of damage on transport processes in concrete, Constr. Build. Mater. 24 (9) (2010) 1638–1648.
[29] J. Ožbolt, F. Oršanić, G. Balabanić, M. Kušter, Modeling damage in concrete caused by corrosion of reinforcement: coupled 3D FE model, Int. J. Fract. 178 (1–2) (2012) 233–244.
[30] J. Ožbolt, F. Oršanić, G. Balabanić, Modeling pull-out resistance of corroded reinforcement in concrete: coupled three-dimensional finite element model, Cem. Concr. Compos. 46 (2014) 41–55.
[31] C. Van Steen, T. Van Beirendonck, R. Vrijdaghs, M.A.N. Hendriks, E. Verstrynge, A two-phased modelling approach for corrosion-induced concrete cracking and bond deterioration in reinforced concrete, Eng. Struct. 294 (2023).
[32] DianaFEA, *Diana User's Manual, Release 10.5.* DIANA FEA BV, 2022.
[33] K. Lundgren, Bond between ribbed bars and concrete. Part 1: modified model, Mag. Concr. Res. 57 (7) (2005).
[34] K. Lundgren, Bond between corroded reinforcement and concrete, in: Department of Structural Engineering, 3, Chalmers University of Technology, Sweden, 2001, p. 2001. Report No. 00.
[35] CEN, Eurocode 2: design of concrete structures-part 1–1: general rules and rules for buildings. 2005: Brussels.
[36] M. Słowik, E. Błazik-Borowa, The Influence of Aggregate Size on the Width of Fracture Process Zone in Concrete Members, in Brittle Matrix Composites 9. 2009. p. 429–438.
[37] S.J. Williamson, L.A. Clark, Effect of corrosion and load on reinforcement bond strength, Struct. Eng. Int. 12 (2) (2018) 117–122.
[38] G. Malumbela, P. Moyo, M. Alexander, A step towards standardising accelerated corrosion tests on laboratory reinforced concrete specimens, J. South Afr. Inst. Civ. Eng. 54 (2) (2012) 78–85.
[39] W. Zhang, R. François, L. Yu, Influence of load-induced cracks coupled or not with top-casting-induced defects on the corrosion of the longitudinal tensile reinforcement of naturally corroded beams exposed to chloride environment under sustained loading, Cem. Concr. Res. 129 (2020).
[40] S. Robuschi, Natural corrosion in reinforced concrete structures, Chalmers University of Technology, Gothenburg, Sweden, 2021.